Structural dynamics of incommensurate charge-density waves tracked by ultrafast low-energy electron diffraction F

G. Storeck (iD), J. G. Horstmann (iD), T. Diekmann, S. Vogelgesang, G. von Witte (iD), S. V. Yalunin, K. Rossnagel (iD), and C. Ropers (iD)

COLLECTIONS

F   This paper was selected as Featured

View Online   Export Citation   CrossMark

Structural dynamics of incommensurate charge-density waves tracked by ultrafast low-energy electron diffraction ⓕ

G. Storeck,[1,a] ⓘD J. G. Horstmann,[1] ⓘD T. Diekmann,[1] S. Vogelgesang,[1] G. von Witte,[1] ⓘD S. V. Yalunin,[1]
K. Rossnagel,[2,3] ⓘD and C. Ropers[1,4,b] ⓘD

AFFILIATIONS

[1]4th Physical Institute, Solids and Nanostructures, University of Göttingen, 37077 Göttingen, Germany
[2]Institute of Experimental and Applied Physics, Kiel University, 24098 Kiel, Germany
[3]Ruprecht Haensel Laboratory, Deutsches Elektronen-Synchrotron DESY, 22607 Hamburg, Germany
[4]Max Planck Institute for Biophysical Chemistry (MPIBPC), Göttingen, Am Fassberg 11, 37077 Göttingen, Germany

[a]gero.storeck@uni-goettingen.de
[b]Author to whom correspondence should be addressed: cropers@gwdg.de

ABSTRACT

We study the non-equilibrium structural dynamics of the incommensurate and nearly commensurate charge-density wave (CDW) phases in
$1T$-TaS$_2$. Employing ultrafast low-energy electron diffraction with 1 ps temporal resolution, we investigate the ultrafast quench and recovery
of the CDW-coupled periodic lattice distortion (PLD). Sequential structural relaxation processes are observed by tracking the intensities of
main lattice as well as satellite diffraction peaks and the diffuse scattering background. Comparing distinct groups of diffraction peaks, we
disentangle the ultrafast quench of the PLD amplitude from phonon-related reductions of the diffraction intensity. Fluence-dependent relax-
ation cycles reveal a long-lived partial suppression of the order parameter for up to 60 ps, far outlasting the initial amplitude recovery and
electron-phonon scattering times. This delayed return to a quasi-thermal level is controlled by lattice thermalization and coincides with the
population of zone-center acoustic modes, as evidenced by a structured diffuse background. The long-lived non-equilibrium order parameter
suppression suggests hot populations of CDW-coupled lattice modes. Finally, a broadening of the superlattice peaks is observed at high flu-
ences, pointing to a non-linear generation of phase fluctuations.

I. INTRODUCTION

The spontaneous breaking of a continuous symmetry is a funda-
mental concept of physics with broad relevance in such diverse areas
as particle physics,[1] cosmology,[2,3] and condensed matter physics.[4,5]
An essential consequence of this symmetry breaking is the emergence
of new amplitude and phase excitations of the fields considered, exem-
plified in the Higgs mechanism[6] and massless Nambu–Goldstone
bosons,[7,8] respectively. Moreover, the degenerate ground state of such
systems allows for non-trivial topological states, as in the case of mag-
netic vortices.[4]

Electron–lattice interaction is an important source of symmetry
breaking in solids, most prominently in superconductivity and the for-
mation of charge-density wave (CDW) phases.[9–12] Specifically, CDWs
constitute a periodic modulation of the charge density by electron–hole

pairing,[12] coupled to a periodic lattice distortion (PLD)[13–15] and an
electronic gap.[16–19] The emergence, correlations, and fluctuations of
symmetry-broken CDW states can be revealed in the time domain
by ultrafast measurement techniques. In this way, quenches of the
electronic gap coupled to coherent amplitude oscillations,[20–26] light-
induced PLD dynamics,[27–30] and phase transitions have been investi-
gated.[20,31,32] In particular, ultrafast structural probes trace changes of
structural symmetry[33,34] and long-range ordering following a phase
transformation.[35,36]

However, while the initial quench and coherent amplitude
dynamics of CDW systems following short-pulsed excitation are
rather well characterized,[20,21,23–26] the subsequent paths to thermal
equilibrium, including the roles of different collective modes in re-
establishing a thermal CDW state, are far less understood. In

particular, a sensitive structural probe is required to study the interplay of CDW-coupled excitations and regular phonons.

Here, we employ ultrafast low-energy electron diffraction (ULEED), a recently developed surface-sensitive structural probe,[35,37–39] to give a comprehensive account of the non-equilibrium structural dynamics of the incommensurate (IC) charge-density wave phases at the surface of $1T$-TaS$_2$. Harnessing the sensitivity of ULEED to the out-of-plane periodic lattice displacements of the sulfur atoms, we isolate the dynamics of an optically induced amplitude quench from a multi-stage excitation of phonons. Following a rapid partial recovery, we observe a surprisingly long-lived non-thermal amplitude suppression that equilibrates only after approximately 60 ps. Energy transfer to acoustic phonons is required to re-establish a thermal value of the PLD amplitude, suggesting that transient populations of collective CDW modes have a lasting impact on the structural order parameter.

II. MATERIALS SYSTEM AND EXPERIMENTAL APPROACH

In this work, we study one of the most prominent CDW systems, $1T$-TaS$_2$, which is part of the class of transition metal dichalcogenides. The atomic structure of this material consists of weakly interacting S–Ta–S trilayers,[40,41] in which the tantalum atoms are octahedrally coordinated between the sulfur atoms [Fig. 1(a)]. This compound has attracted much attention for its various CDW phases,[12,40–42] excitations[21,24–27,43] [Fig. 1(c)], and correlation effects,[44–46] serving as a model system to study, for example, Peierls-

vs Mott-type metal–insulator transitions,[23,47] pressure-induced superconductivity in coexistence with CDWs,[48] transitions to metastable "hidden" CDW states,[32,49] the emergence of complex orbital textures,[50] or quantum spin liquid behavior.[51]

The material exhibits multiple temperature-dependent phases [Fig. 1(f)] with characteristic lattice deformations coupled to electronic structure changes.[40,47,52] Starting from a metallic phase with an undistorted trigonal structure [Fig. 1(a)] above 543 K, the system undergoes a sequence of CDW transitions, forming a commensurate (C) (Mott-insulating) state below 187 K. At intermediate temperatures, two incommensurate phases are found, namely the so-called "nearly commensurate" (NC) phase (187–353 K), exhibiting commensurate patches separated by discommensurations,[41,53–55] and a homogeneous, fully incommensurate (IC) structure [Fig. 1(b)] between 353 K and 543 K. The periodic lattice distortions in these phases are characterized by primarily in-plane and out-of-plane displacements of the tantalum and sulfur atoms, respectively [Figs. 1(b) and 1(c)]. Ultrafast transitions between and manipulation of these phases, as well as their collective modes [Fig. 1(d)], have been observed in various diffraction and spectroscopy studies.[20,21,23–27,33,35,43,56–61]

In our experiments, we employ pulses of electrons at low energies, typically in the range of 40–150 eV, to probe the structural evolution of the NC and IC states in backscattering diffraction. ULEED[35,37–39] allows us to trace the changes of the diffraction pattern in the time domain, following intense fs-laser illumination [red pulse in Fig. 1(e)]. In this optical-pump/electron-probe scheme, excitation and relaxation processes are sampled by varying the time delay t
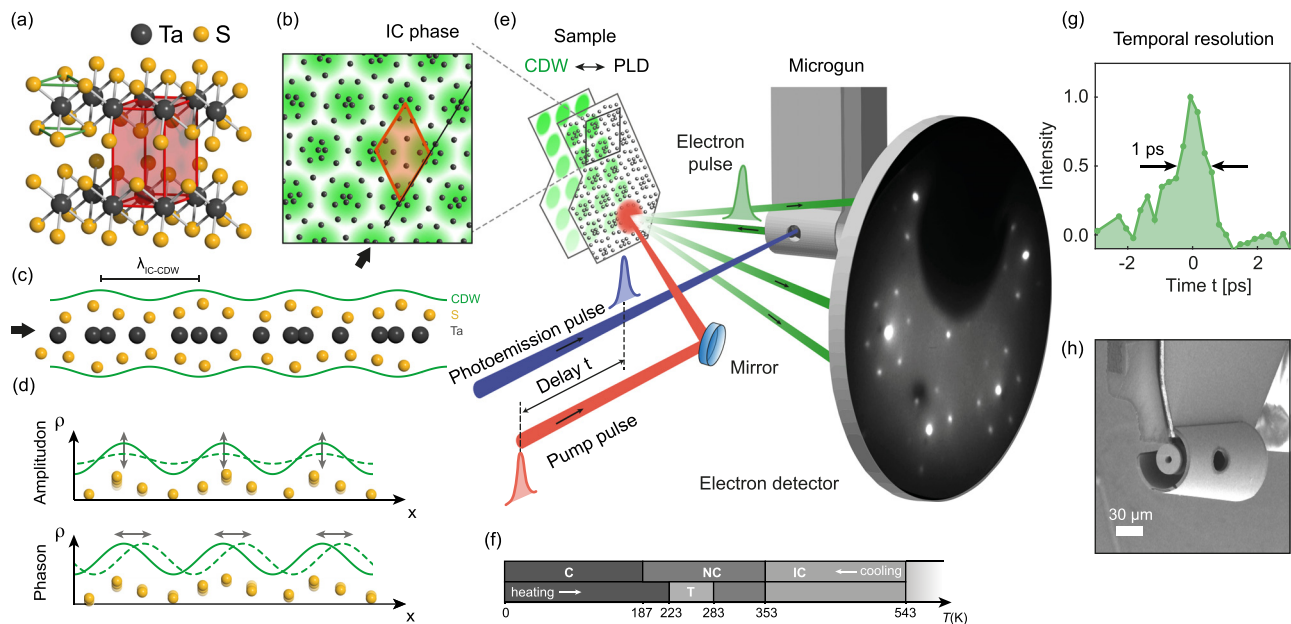
FIG. 1. Materials system and experimental setup. (a) Layered transition metal dichalcogenide $1T$-TaS$_2$ exhibiting a trigonal crystal structure in the high-temperature phase (green lines: octahedral $1T$-coordination; red: unit cell). (b) Top view of the incommensurate (IC) CDW phase illustrating the charge density (green), distorted lattice (black dots: Ta atoms, displacements exaggerated), and superstructure unit cell (orange). (c) Side view of a single S–Ta–S trilayer, illustrating the out-of-plane periodic lattice displacements of the sulfur atoms (exaggerated). (d) 1D sketch of CDW amplitude and phase excitations and corresponding lattice fluctuations. (e) Schematic of the experimental setup, showing ultrafast LEED in a backscattering geometry. Ultrashort electron pulses (green) from a nanofabricated electron gun probe the dynamical evolution of the laser-excited surface structure. (f) Temperature-dependent CDW phases. (g) Achieved electron pulse duration of 1 ps (see Appendix A for details). (h) Scanning electron micrograph of the miniaturized electron gun.

between the optical pump pulse (red) and the photoemission pulse (blue) generating the electron probe (green). Reducing electron pulse broadening by short propagation lengths, a miniaturized electron gun [Fig. 1(h)][38] allows for a temporal resolution of 1 ps [Fig. 1(g)]. Further experimental details are provided in Appendix A (Fig. 7).

To facilitate the discussion, we focus the presentation on the response of the IC phase, which has not been studied by ultrafast diffraction, and provide a comprehensive dataset of related observations for the NC phase in Appendix B.

The IC phase exhibits a triple-Q CDW/PLD, with lattice displacements for each unit-cell atom of the form[62,63]

$$\mathbf{u}(\mathbf{L}) = \sum_{i=1,2,3} \mathbf{A}_i \sin\left(\mathbf{Q}_i \cdot \mathbf{L} + \varphi_i\right) \quad (1)$$

for lattice sites $\mathbf{L}$, CDW wavevectors $\mathbf{Q}_i$, and phases φ_i. The CDW/PLD texture of a "dot-lattice" arises for the phasing condition $\sum_i \varphi_i = 0$, and for symmetry reasons, the individual plane wave components share a common amplitude $A = |\mathbf{A}_i|$. The PLD at a wavelength $\lambda_{IC} = 3.53a$ (a: lattice constant) leads to characteristic arrangements of satellite peaks[64,65] around the main lattice diffraction spots, seen in the ULEED pattern displayed in Fig. 2(c). As the IC state wave vectors are collinear to the lattice vectors, the satellites are located on the lines connecting the main reflexes. Due to the harmonic (and weak) structural modulation,[53,54] only first-order satellites are observed, with an intensity[64] $I_{sat} \sim |J_1(\mathbf{s} \cdot \mathbf{A}_i)|^2 \sim A^2$ ($\mathbf{s}$: scattering vector). We note that in this energy range, LEED is a very efficient structural probe of the PLD because (i) backscattering diffraction is dominated by the sulfur sublattice and (ii) the large out-of-plane momentum transfer enhances the sensitivity to out-of-plane displacements.

We study the excitation and relaxation of the IC and NC phases, without driving the system across a phase transition.[29,33,35,36,53,62] The

dynamics of this incommensurate Peierls system can be discussed based on a simplified picture of three coupled subsystems, namely, the electronic system exhibiting a gapped band structure [Fig. 2(a), top], the collective amplitude and phase excitations around the symmetry-broken CDW ground state (center),[12] and the ordinary lattice modes far from the CDW wavevector in reciprocal space, i.e., regular phonons (bottom).

It is widely established that electronic excitation by an ultrashort laser pulse induces a carrier population above the bandgap, which results in a quench of the CDW/PLD amplitude that recovers upon carrier cooling by electron-phonon scattering.[24,27,43] The corresponding sequence of relaxation processes involving the three subsystems causes characteristic changes to the diffraction intensities of the satellite peaks and the main peaks (intensity I_{main}). Specifically, for small PLD amplitudes, the peak intensities are expected to scale as[64–67]

$$I_{sat} \sim A^2\, e^{-2W_\varphi}\, e^{-2W_s}, \quad (2)$$

$$I_{main} \sim \left(1 - c_s A^2\right) e^{-2W_s}. \quad (3)$$

These expressions reflect that a light-induced quench of the mean PLD amplitude A will lead to a redistribution of intensity from the satellites to the main peaks.[27,28,68] Different main reflexes are sensitive to the PLD to a varying degree, which requires the introduction of the factor c_s that depends on the momentum transfer $\mathbf{s}$. Inelastic scattering by generated phonons transfers intensity from the reflexes to a diffuse background [Fig. 2(b)],[69–72] leading to a peak suppression by a Debye–Waller factor $\exp(-2W_s)$.[67,69] The general form of the exponent[67,69] $W_s \sim \sum_{ph} (\mathbf{s} \cdot \mathbf{u}_{ph})^2$ sums over the momentum transfer projected onto phonon displacements $\mathbf{u}_{ph}$ in various branches. According to Overhauser,[64] phase fluctuations result in the additional "'phason Debye–Waller factor" $e^{-2W_\varphi} = e^{-\langle \varphi^2 \rangle}$, which only affects the satellite spots and also causes diffuse scattering in the vicinity of the satellite peaks.[66,73] Finally, dislocation-type topological defects in the CDW
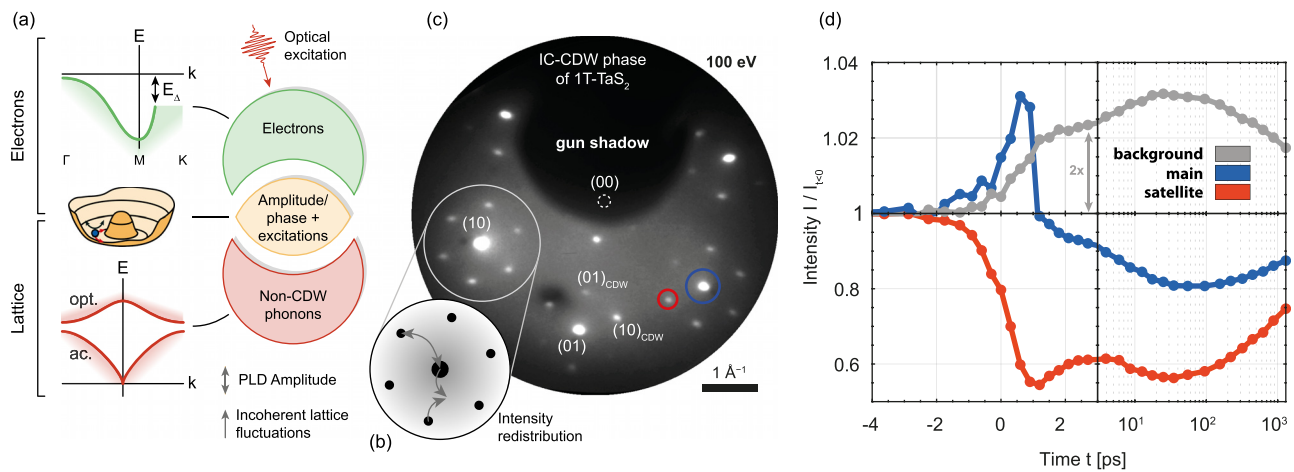
FIG. 2. Dynamics and excitations in CDW systems influencing diffraction. (a) Electron and lattice subsystems (right) governing CDW dynamics. Gapped band structure (top, left), symmetry broken CDW state with phase and amplitude excitations (middle), and non-CDW phonons (bottom). (b) Changes in average amplitude and all lattice excitations (CDW and non-CDW) lead to a redistribution of intensity in the electron diffraction pattern. (c) Diffraction pattern of the IC phase of 1T-TaS$_2$ showing main lattice reflexes and first-order PLD-induced satellites (integration time: 90 s; electron energy: 100 eV). (d) Time-dependent measurement of reflexes [blue and red circles in (c)] and diffuse background (fluence $F = 2.5$ mJ/cm^2). The main lattice signal is averaged over (10) and (-1 1) spots (blue), the satellite signal over several reflexes. Curves are normalized to the signal at negative times.

may broaden the superlattice peaks and also reduce the PLD in the dislocation core.[35,59]

III. RESULTS AND ANALYSIS

Our ULEED experiments directly show the characteristic diffraction changes mentioned above: in the exemplary data displayed in Fig. 2(d), a main lattice peak (blue) exhibits a transient intensity increase after the pump pulse, before experiencing an initially rapid and then slowed suppression to a minimum at $t = 60$ ps. The satellite peaks (red), on the other hand, are first suppressed, before approaching a similar trend as the main peak beyond approximately 10 ps. Both the satellite and main peak intensities are significantly reduced by phonon populations.[69] These are evident in the diffuse background (gray), which mirrors the suppression of the reflexes, with a step-like increase in the first ps and a slower rise to a maximum at the delay of 60 ps. The initial step can be interpreted as the excitation of a broad population of optical and acoustic phonons on the timescale of electron–phonon energy relaxation (<1 ps),[26] while the slower timescale corresponds to phonon–phonon equilibration[74] and the population of low-energy acoustic modes. LEED intensities are rather sensitive to the large amplitudes of low-frequency modes, particularly those with out-of-plane polarization. Specifically, phonon modes with out-of-plane displacements $\mathbf{u}_{ph}$ have a more pronounced Debye–Waller factor due to the backscattering geometry with a primarily out-of-plane scattering vector of the electron. In addition, these modes exhibit comparatively slow phase velocities, as is typical for layered van der Waals materials.[75] Thus, the prominent main lattice suppression evolving over tens of picoseconds primarily stems from the increasing population of low frequency acoustic modes modulating the layer distance.

These strong Debye–Waller factors complicate an analysis of the temporal evolution of the amplitude quench. On the other hand, our experimental data show that different reflexes share a common phonon-induced peak suppression. In Secs. III A and III B, we pursue two approaches of disentangling the dynamics of the structural order parameter from the phonon population, exploiting the different sensitivities of two inequivalent classes of main lattice reflections to the PLD (Sec. III A) and the direct sensitivity of the satellite reflexes to the PLD (Sec. III B).

A. Amplitude analysis based on main lattice reflexes

Concerning the time-dependent peak intensity, the main reflexes fall into two different groups. Whereas all five visible main peaks show a suppression opposite to the increase in the diffuse background [Fig. 3(a)], we find that the transient amplitude signal is prominent only in the (1 0) and (−1 1) peaks, while it is largely absent in the (01), (−10), and (1 −1) peaks [see also difference maps in Fig. 3(b)].[76] These two groups of peaks are crystallographically distinct, and the peaks within each group are equivalent in the effective threefold symmetry of the 1T structure.[77] The different sensitivities of the peak intensities to the PLD are a particular feature of LEED, as described in the following.

In the electron energy range of 70–110 eV, diffraction intensities are mainly governed by scattering from sulfur atoms due to large atomic scattering factors.[41,77] As a result of the CDW-induced contraction of the tantalum sublattice, the sulfur atoms predominantly exhibit out-of-plane displacements. In backscattering, the opposing directions for the displacements in the upper and lower sulfur layers
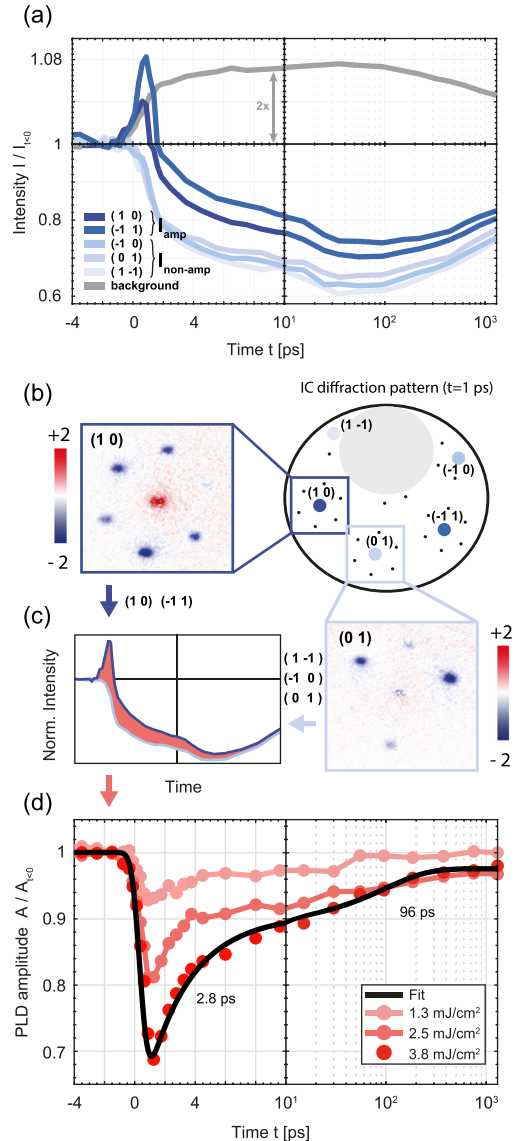

FIG. 3. Amplitude dynamics of the PLD obtained from main lattice reflexes. (a) Time-dependent intensity of visible main lattice reflexes and integrated background intensity, for a fluence of $F = 3.8$ mJ/cm^2. Two inequivalent classes of spot groups are found, featuring a strong (dark blue) and a weak (light blue) sensitivity to the amplitude quench. (b) Sketch of the IC diffraction pattern, and parts of the difference diffraction image ($I_{t=1ps} − I_{t<0}$) around the (10) and (01) main reflexes (insets). (c) Schematic comparison of peak intensities in the spot groups. The red area highlights different sensitivities to the PLD. (d) Extracted PLD amplitude quench and relaxation (see also Appendix A) for three fluences, showing a rapid and a slower relaxation component (time constants from a biexponential fit (black line) to the highest fluence data: (2.8 ± 0.3) ps and (96 ± 3) ps).

within each S–Ta–S trilayer[41,77] [Fig. 1(c)] lead to an interference with enhanced or suppressed sensitivity of the two groups of main lattice peaks to the lattice distortion. This feature is expected in all CDW phases of 1T-TaS$_2$, which share the phasing condition mentioned above [compare Fig. 1(b)]. Experimentally, we found the same trend

in experiments on the NC phase (see Appendix B), which exhibits different wavevectors but the same phasing between the three CDWs. In order to further corroborate these findings and consider the importance of multiple scattering in LEED, we conducted dynamical LEED simulations for a PLD of varying amplitudes and as a function of the electron beam energy (see Appendix F). In these simulations, for computational reasons, the commensurate modulation was employed, taking quantitative displacements from a recent LEED reconstruction.[77] Importantly, the dynamical LEED simulations qualitatively reproduce our experimental findings of different sensitivities to the PLD by the two groups of main lattice peaks. Moreover, the simulations predict an energy-dependent and strongly reduced PLD sensitivity at an electron energy of 80 eV. Indeed, experiments at this lower energy show that the transient increase in the main peak is generally much weaker (see additional data in Appendix C).

We employ these different sensitivities to the PLD to derive a phonon-corrected amplitude signal. Specifically, we remove the phonon-induced Debye–Waller suppression by normalizing the intensity of the PLD-sensitive peaks to that of the weakly sensitive peaks [Fig. 3(c); see Appendix A for details]. The resulting phonon-corrected amplitude suppression is displayed in Fig. 3(d) for three pump fluences. In each case, the amplitude exhibits a rapid initial quench (within our temporal resolution) and a recovery with an exponential time constant of about 3 ps. The re-establishment of the amplitude is, however, incomplete, slowing down considerably beyond 4 ps and lasting well into the range of tens to one-hundred picoseconds.

B. Amplitude analysis based on satellite reflexes

We now aim at characterizing the evolution of the mean amplitude based on the satellite peak intensities, again removing a time-dependent phonon Debye–Waller factor. To this end, we compare the intensities of the main peaks with weak PLD sensitivity to the satellite peaks. In Fig. 4(a), we plot the logarithm of these intensities (normalized to the signal at $t < 0$), divided by the fluence. For all three fluences, the traces of the main lattice peaks collapse to a single universal curve (blue), illustrating the phonon-induced Debye–Waller suppression $W_{\mathbf{s}}$ and its proportionality to fluence. The satellite peaks show a non-exponential fluence dependency in their suppression and recovery. At low fluences, however, where only a minor amplitude quench is induced, the satellite peak suppression closely follows that of the main peaks. We use this information to derive a phonon-corrected amplitude signal from the satellite peaks (see Appendix A). Figure 4(b) shows the resulting amplitude evolution. For this graph, the satellite intensities were integrated over circular masks in the diffraction pattern (width of $\Delta k_{sat} = 0.36$ Å^{-1}), therefore including also electrons scattered by a small angle from the reflex. We find a very similar behavior as from the main peak analysis (see Sec. III A), namely, a rapid and fluence-dependent quench, a fast initial recovery, and a rather persistent partial suppression, and we therefore consider this quantity as representative for the evolution of the amplitude A.

A somewhat different curve is obtained by utilizing not the area-integrated intensity but the maximum intensity on top of the diffraction spot [bottom graph in Fig. 4(b)]. Whereas the maximum and integrated intensities behave similarly at low fluence, at the highest fluence, the suppression of the maximum intensity exceeds that of the integrated intensity (gray curve from integrated intensity shown again
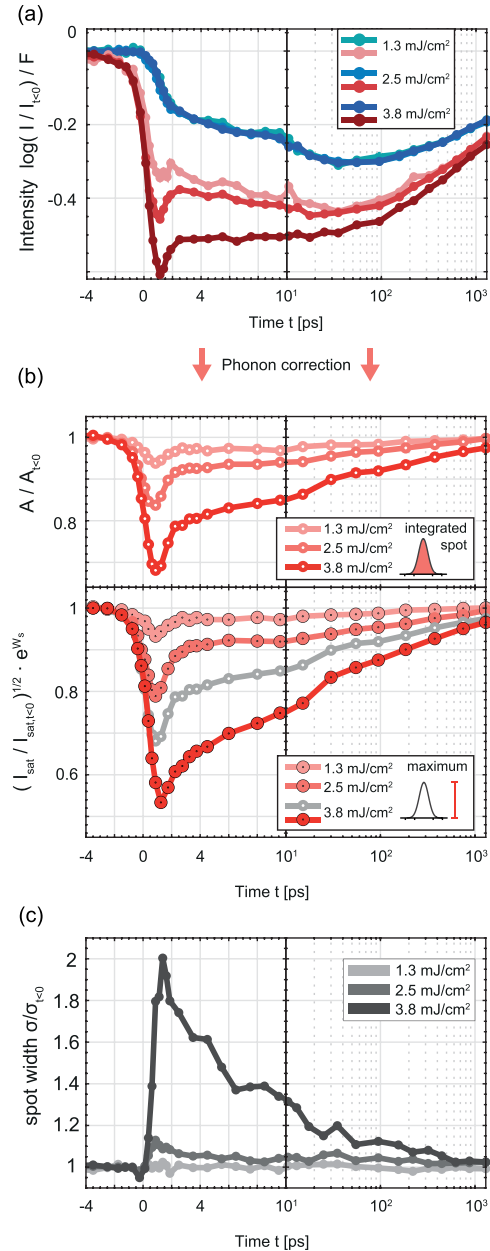
FIG. 4. Amplitude dynamics of the PLD obtained from satellite reflexes. (a) Logarithm of the normalized main lattice and satellite peak intensities (mean value), divided by fluence, vs time delay. While the main peak intensities (blue) collapse to a single curve due to the exponential (in fluence) Debye–Waller-type suppression, the satellite intensities (red) show a strong fluence-dependent behavior for early times, before converging for long time delays. (b) Phonon-corrected PLD amplitude obtained from integrated (top) and maximum (bottom) satellite intensities. (c) Fluence-dependent azimuthal spot width σ vs time.

for comparison). Moreover, the recovery of the maximum proceeds more gradually than the integrated intensity.

The difference between the evolution of the integrated and maximum intensities implies a change in the diffraction peak shape, which

is analyzed in Fig. 4(c). Plotting the azimuthal width of the diffraction peak, we find a significant time-dependent broadening for the highest fluence.

This effective broadening may be a result of several phenomena: (i) diffuse scattering to the wings of the peak by low-energy phase excitations[14] will suppress the reflex maximum via the phason Debye–Waller factor $\exp(-2W_\varphi)$ while largely maintaining the integrated intensity. (ii) An overall peak broadening from reduced correlation lengths will arise from the generation of CDW dislocation-type topological defects.[35,59] Except for the amplitude suppression in the dislocation core, this broadening also preserves the integrated intensity. At this point, we cannot rule out either scenario, and a more detailed spot profile analysis or higher momentum resolution may be required to further elucidate the different contributions.

C. Non-equilibrium dynamics of the amplitude

The incomplete recovery and persistent suppression of the PLD amplitude, independently obtained from the main [Fig. 3(d)] and satellite [Fig. 4(b)] reflexes, warrant further investigation. This implies that the system is either thermalized at a higher temperature with reduced equilibrium amplitude[28] or, alternatively, that non-equilibrium dynamics inhibit the recovery of the order parameter. It was previously suggested for the NC phase that the rapid recovery results in a thermalized system at elevated temperature.[27] Specifically, this would entail equilibrium between the electronic and different structural degrees of freedom after approximately 4 ps.

As shown in the following, we have evidence for a sustained nonthermal suppression of the order parameter. In Fig. 5, we consider in more detail the path to thermal equilibrium. An instructive depiction is obtained by plotting the main and satellite intensities against each other, resulting in cyclic trajectories in a two-dimensional plane [Fig. 5(a)], traced out over time in a clockwise fashion. At long delays (beyond 100 ps), the curves for all fluences follow a universal path (dashed line) representing a thermalized system at elevated temperatures, cooling down. Different trajectories reach the same combination of intensities at different times. For instance, the high-fluence trajectory exhibits the same combination of intensity suppressions at 1500 ps as the intermediate fluence at a somewhat earlier time of 290 ps [black circle in Fig. 5(a)]. Once the trajectory reaches this line, the surface is in local thermal equilibrium, characterized by a single temperature, and the satellite peak suppression is composed of a Debye–Waller factor and a thermal reduction of the amplitude. The further progression of the system, i.e., its cooling, is governed by thermal diffusion to the bulk.

All points *displaced* from the dashed line represent deviations from a thermal state, with the distance being a very sensitive measure of the structural non-equilibrium. For example, within the first picosecond after the excitation (dark segments of the curves), the rapid quench of the order parameter causes a reduction of satellite intensity and a moderate enhancement of the main lattice signal, with a fluence-dependent maximum displacement from thermal equilibrium (the corresponding curves for the main peaks insensitive to the amplitude are found in Appendix D). The recovery to the thermal state now proceeds through various stages and in a fluence-dependent manner. After about 4 ps (see marks), the fast component of the amplitude recovery is completed [cf. Fig. 3(d), compare also Ref. 74].[78] However, the system remains far from the equilibrium state, i.e., exhibits a

(a)

(b)
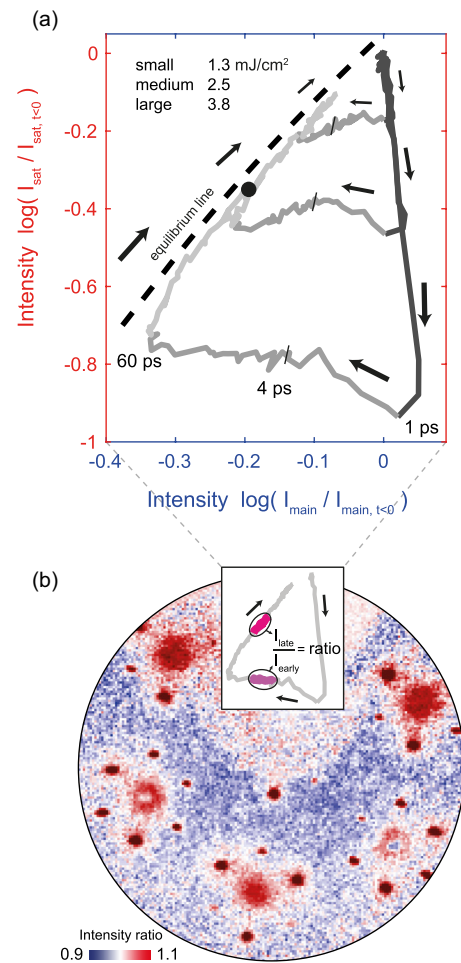
Intensity ratio
0.9   1.1

FIG. 5. Path to equilibrium. (a) Intensities of satellite and main peaks (with PLD sensitivity) plotted against each other, leading to cyclic trajectories in a 2D plane with varying sizes. Note that all curves reach a common equilibrium line after approximately 60 ps. The gray color scale highlights certain time intervals (dark gray: 0–1 ps, medium, gray: 1–60 ps, and light gray: 60–1500 ps). The same combination of intensity suppressions is found for different fluences at different times (the black circle corresponds to 1500 ps/290 ps at high/intermediate fluence). (b) Ratio of time-integrated frames exhibits prominent pedestals around diffraction peaks, pointing to an enhanced acoustic phonon population on the equilibrium line. Late frames (dark magenta in the inset, $t = 790, ..., 1500$ ps) are divided by early frames (light magenta in the inset, $t = 4.5, ..., 10$ ps).

lower-than-thermal satellite intensity. Interestingly, for all curves, a surprisingly long time of approximately 60 ps is required to reach the thermal state. This depiction directly shows that the persistent amplitude suppression discussed in Figs. 3(d) and 4(b) is, in fact, not of a thermal nature and that we have a pronounced deviation from equilibrium between the degrees of freedom affecting the diffraction intensities.

To identify the origin of this long-lived amplitude suppression, we first note that the time at which the system reaches a thermal amplitude nearly coincides with the strongest suppression of the main lattice peaks. As this time also corresponds to the maximum intensity of the diffuse background [cf. Figs. 2(d) and 3(a)], the full equilibration

of lattice fluctuations appears to be critical in controlling the structural order parameter. In particular, this lattice equilibration induces a significant increase in diffuse background intensity around main lattice peaks [difference image in Fig. 5(b)], directly pointing to the excitation of low-energy acoustic modes near the center of the Brillouin zone.

IV. DISCUSSION

Taken together, these observations indicate the sequence of relaxation processes illustrated in Fig. 6(b), which can be related to the intensity curves [Fig. 4(a)] and the cyclic trajectories introduced above [simplified sketch in Fig. 6(a)]. Within the first picosecond, the optical excitation of the electronic system leads to a CDW amplitude quench and a strong deformation of the potential energy landscape [see insets in Fig. 6(b)], which triggers cooperative motion of the lattice toward its unmodulated state, including the excitation of coherent amplitude modes (stage 1).[26,43] Facilitated by the generation of high-energy lattice modes, the electron system cools down within few ps (stage 2), and as a result, the electronic potential and amplitude partially recover. The remaining PLD suppression in the following stage 3 strongly indicates a substantial population of CDW-coupled lattice excitations [Fig. 6(b), red filling in the bottom inset], such as amplitudons, phasons, and possible dislocation-type topological defects. Remaining non-thermal electronic excitations, on the other hand, can be largely ruled out at these late times, based on results from time- and angle-resolved photoemission spectroscopy.[23,24,32,43,79] While it is known that phonon equilibration may take tens of picoseconds,[80,81] the present observations are significant in the sense that the persistent structural non-equilibrium is found to directly lead to an amplitude suppression via long-lived CDW-coupled excitations.

Both amplitude and phase modes are expected to be rather efficiently excited by the optical pump, either directly by the deformation of the electronic potential (amplitude modes)[25] or by electron lattice scattering between gap regions [Fig. 6(d)]. Specifically, Fermi surface nesting is expected to result in a high probability of scattering events with a momentum transfer around the CDW wavevector Q [Fig. 6(d), left]. Subsequent cooling of the carrier temperature below the energy scale of the electronic gap will effectively suppress these inelastic scattering pathways [Fig. 6(d), right] and decouple the subsystems [Fig. 6(c)], contributing to the persistent amplitude suppression in stage (3). Full lattice thermalization and the excitation of zone-center acoustic modes are then only achieved after 60 ps, from which point the equilibrated system cools down (stage 4).

Let us consider the possible roles of different CDW excitations in the long-lived amplitude suppression, namely, amplitudons, phasons, and CDW dislocation defects. Spatiotemporal variations of the amplitude and phase affect the observable value of A. Specifically, amplitudons represent amplitude oscillations ΔA around an equilibrium amplitude A_0, leading to an observed average value of $\langle A_0 + \Delta A \rangle$. By an anharmonicity of the electronic potential, these oscillations become asymmetric, and a high population of amplitudons can reduce the value of A. In the case of phasons, despite early theoretical and experimental work,[13,14,64,65,82–86] a unifying picture has not been reached, and recent assignments of their contribution in diffraction studies range from largely negligible[68] to dominant.[73] While our results do not definitely resolve this issue, the redistribution of scattering intensity near the satellite peaks suggests significant spatial or spatiotemporal phase distortions.

CDW dislocation defects should also be considered as a possible cause for the long-lived order parameter suppression, as they have
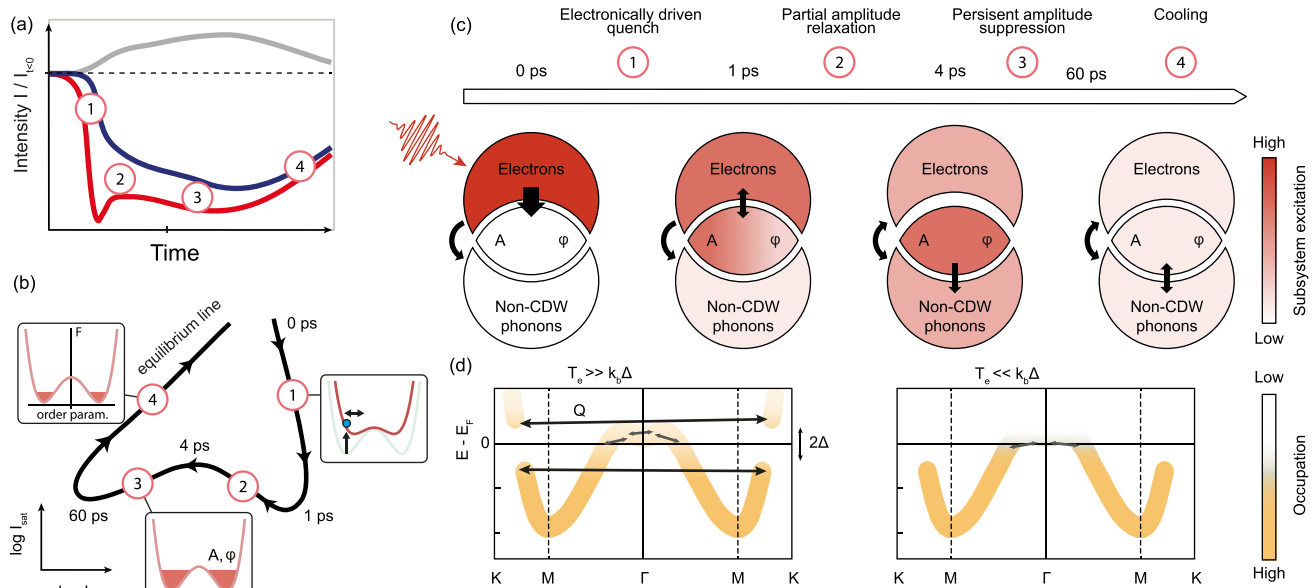

FIG. 6. Linking relaxation pathways to CDW/PLD dynamics. (a) and (b) Simplified sketches of Figs. 2(d) and 4(a), respectively, highlighting four phases of the relaxation process observed in the data. (c) Illustration of the sequential relaxation process and the excitation levels of the three subsystems. The color shade represents the energy content/temperature, and black arrows indicate energy flow. (d) Simplified electronic band structure and populations (saturation of the orange line) for high (left) and low (right) electronic temperatures. Arrows indicate electron-lattice scattering processes. Scattering between gap regions (momentum transfer Q) is suppressed for reduced electronic temperatures.

been observed as a consequence of phase transitions, e.g., in $1T\text{-TaS}_2$[35] or LaTe_3.[59,87] The fact that we find a significant spot broadening of the satellites [Fig. 4(c)] most strongly at high fluences suggests a non-linear dependence of phase fluctuations. This would be consistent with either CDW dislocations generated by critical phase fluctuations or a parametric decay of amplitudons into phase modes, as previously proposed.[22]

V. CONCLUSIONS

The impact of fluctuations on symmetry breaking transitions has long been considered, for example, in the Peierls instability.[88–91] Providing a time-domain view of the structural relaxation pathways, the present measurements highlight the impact of long-lived structural non-equilibrium to the order parameter.

The general mechanism of amplitude suppression by CDW-coupled modes should apply also to other phases and systems. Indeed, measurements in the NC phase feature a similar behavior as the IC phase (Appendix B). Despite differences in symmetry, CDW wavevectors, and electronic gaps, both phases exhibit closely related amplitude and phase excitations, as pointed out by Nakanishi and Shiba.[92]

Relevant further questions pertain to the possible mechanisms of generating phasons and dislocation-type topological defects, as well as their coupling to regular lattice modes. Also, the link between fluctuation modes and the creation and relaxation of metastable states[32,49] and the influence of partial and full commensurability in different CDW states call for further investigation. Additional insights may be gained by investigating the ultrafast phase transitions between different CDW states[35,36,56] and the populations of amplitude and phase modes in the nascent state after transition.

Considering methodical aspects, this work represents the first comprehensive study employing ULEED with a temporal resolution of 1 ps. Future investigations using ULEED will enable a quantitative analysis of the three-dimensional structural evolution based on time- and energy-dependent diffraction. Moreover, the method is applicable to a wide variety of other surface systems and low-dimensional structures, harnessing its strengths of high momentum resolution, efficient scattering, and enhanced sensitivity to lattice fluctuations.

APPENDIX A: METHODS

1. Experimental details

Here, we briefly describe our experimental ULEED apparatus (Fig. 7). The time-resolved measurements are conducted in an ultra-high vacuum chamber (base pressure $p = 5 \times 10^{-11}$ mbar) into which samples are transferred via a load-lock system and cleaved *in situ*. Inside the chamber, the electron source (microgun[38]) and a microchannel plate detector are mounted. A cooled CMOS camera records the detected electron diffraction patterns from outside the UHV chamber.

A femtosecond laser system (Amplifier, NOPA and OPA) generates three femtosecond laser beams of different center wavelengths. An ultraviolet beam (center wavelength of 400 nm) is focused on a nanometric tungsten needle that is embedded inside the microgun[38] generating ultrashort electron pulses via two-photon photoemission. An electrostatic lens assembly controls the
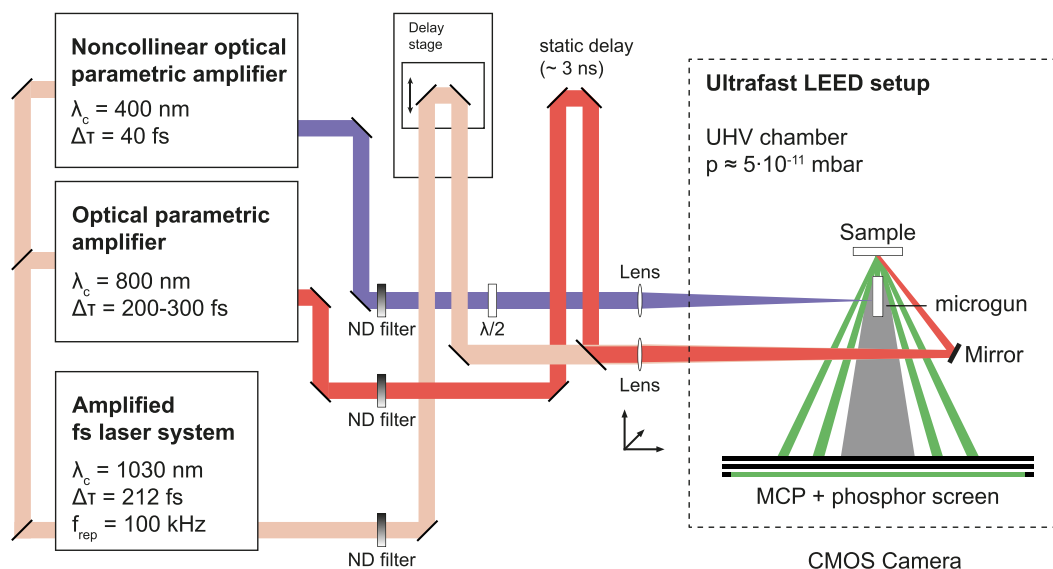

FIG. 7. Schematic of the ultrafast LEED setup.

collimation of the electron beam having an energy range of 40–100 eV. With a gun front diameter of 80 μm and a working distance of around 150 μm, we achieve a temporal resolution of 1 ps and an electron beam diameter of approximately 10 μm at the sample. An upper limit of the technique's temporal resolution is obtained by the derivative of the fastest intensity change in our dataset (suppression of the satellite peak at 100 eV) shown in Fig. 1(g). An infrared beam (center wavelength, 1030 nm) optically excites the sample at specific times controlled by an automated linear delay stage. In order to heat the $1T$-TaS_2 sample and stabilize it in the IC phase slightly above $T \approx 353$ K, a third beam (800 nm) is aligned collinearly with the infrared beam. This pulse is delayed by about 3 ns with respect to the electron and 1030 nm pulses (i.e., it arrives 10 μs before the next pulses) and thus leads to an average increase in sample temperature.

2. Data analysis

The recorded LEED images are preprocessed to correct for minor drifts in-between measurement runs and for distortions caused by local electromagnetic fields and the projection to a flat MCP detector.

In order to obtain time curves [Fig. 2(d)] from the stacks of diffraction patterns, we process the data in a sequence of operations. First, a binary circular mask is laid on top of each individual reflex [Fig. 2(c); blue and red circle, diameter $\Delta k_{main} = 0.6$ Å^{-1} and $\Delta k_{sat} = 0.36$ Å^{-1}, respectively] for each time delay. Second, we fit 2D Cauchy distributions (background: slope and constant offset) to the satellite reflexes and 2D pseudo Voigt profiles (background: slope and constant offset) to the main lattice reflexes, to determine a background profile and subtract it from each spot:
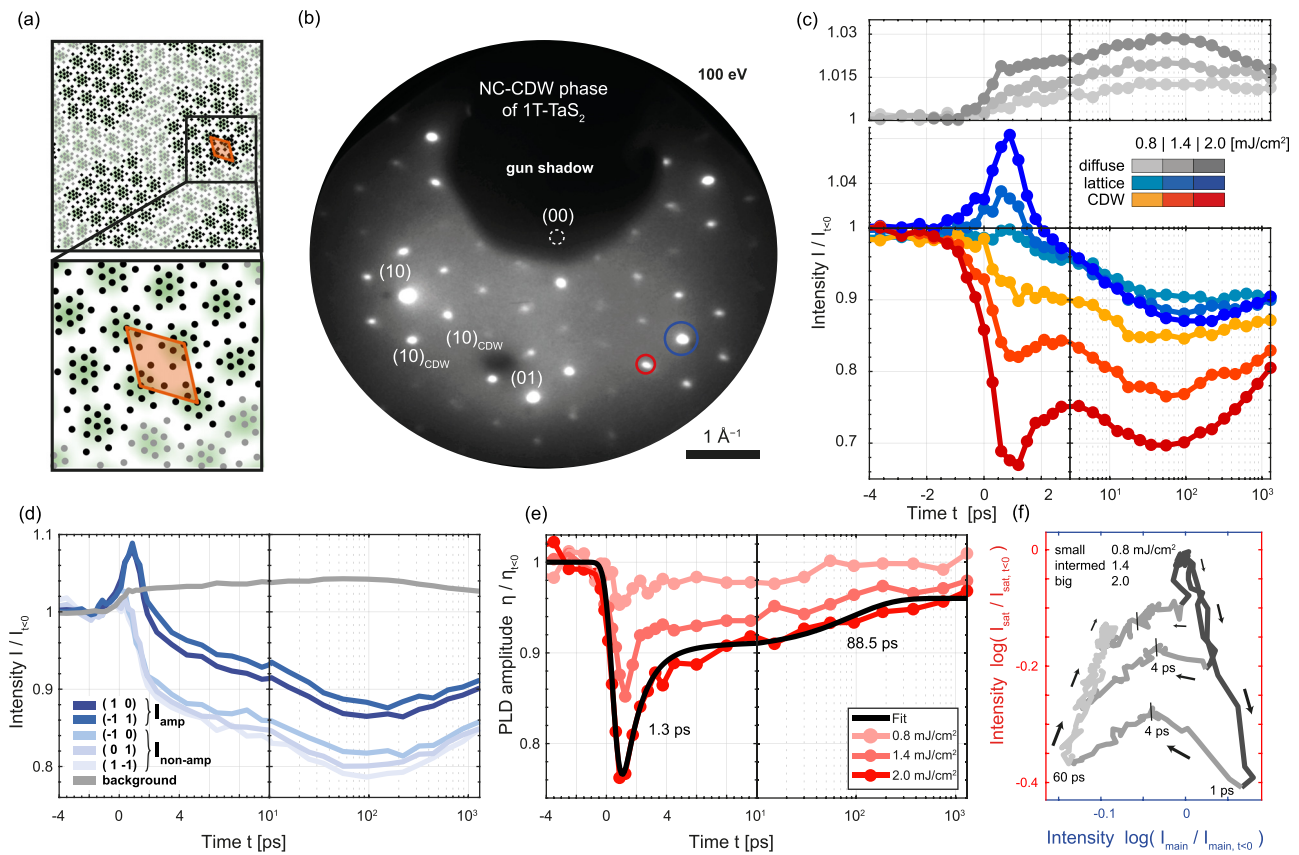

FIG. 8. Measurements in the NC phase for an electron energy of 100 eV. (a) Top view of the nearly commensurate (NC) CDW phase illustrating the charge density (green), distorted lattice (black dots, displacements exaggerated), and superstructure unit cell (orange). (b) Diffraction pattern of the NC phase of $1T$-TaS_2 showing main lattice reflexes and several orders of PLD induced satellites (integration time: 90 s). (c) Time-dependent measurement of reflexes [blue and red circles in (b)] and diffuse background (for three fluences). The main lattice signal is averaged over the (10) and (−1 1) spots (blue), the satellite signal over several reflexes. Curves are normalized to the signal at negative times. (d) Time-dependent intensity of visible main lattice reflexes and integrated background intensity, for a fluence of $F = 2.0$ mJ/cm^2. Two inequivalent classes of spot groups are found, featuring a strong (dark blue) and a weak (light blue) sensitivity to the amplitude quench. (e) Extracted PLD amplitude quench and relaxation for three fluences, showing a rapid and a slower relaxation component [time constants from a biexponential fit (black line) to the highest fluence data: 1.3 ps and 88.5 ps]. (f) Main lattice peak intensities vs satellite peak intensities, leading to cyclic trajectories in a 2D plane with varying sizes. Following a two-stage relaxation, all curves reach a common equilibrium line after approximately 60 ps. The gray color scale highlights certain time intervals (dark gray: 0–1 ps, medium, gray: 1–60 ps, and light gray: 60–1500 ps).

$$C(x,y) = \frac{A}{2\pi\sigma_1\sigma_2} \cdot \left(1 + \left(\frac{x}{\sigma_1}\right)^2 + \left(\frac{y}{\sigma_2}\right)^2\right)^{-3/2}$$
$$+ (a \cdot x + b \cdot y) + C, \qquad \text{(A1)}$$

$$PV(x,y) = A \cdot \left(1 + \left(\frac{x}{\sigma_1}\right)^2 + \left(\frac{y}{\sigma_2}\right)^2\right)^{-3/2}$$
$$+ B \cdot e^{-(x/\sigma_3)^2 - (x/\sigma_4)^2} + (a \cdot x + b \cdot y) + C. \qquad \text{(A2)}$$

Here, the x and y axes correspond to the azimuthal and radial directions (with respect to the main peak) for a given spot. Third, from the background-corrected segment, the average and the maximum intensity (average over brightest 4% within a mask) are determined for each reflex within the mask. The remaining intensity outside the circular masks forms the integrated background. For an improved signal-to-noise ratio, several spot curves are averaged, i.e.,

the satellite curves represent the mean of the 11 brightest reflexes. Furthermore, from the 2D fit functions, we obtain the azimuthal (σ_1) and radial (σ_2) widths for each reflex [Fig. 4(b)].

a. Debye–Waller–corrected amplitude signal

Next, we describe the separation of the amplitude-quench-related intensity changes from Debye–Waller–type peak suppression for the main lattice [Fig. 3(d)] and satellite reflexes [Fig. 4(b)].

The dynamical LEED simulations indicate that there can be considerable differences in the coefficients c_s [Eq. (3)]. Empirically, we find that for the IC phase, the [(0 1), (−1 0), (1 −1)] peaks show a negligible influence of the initial quench ($c_s \approx 0$). In Fig. 3(a), for each fluence, light blue ($c_s \approx 0$) and dark blue curves ($c_s > 0$) are averaged ($I_{\text{non-amp}}$ and I_{amp}). We now use the two peak groups to extract the temporal evolution of A by removing the time-
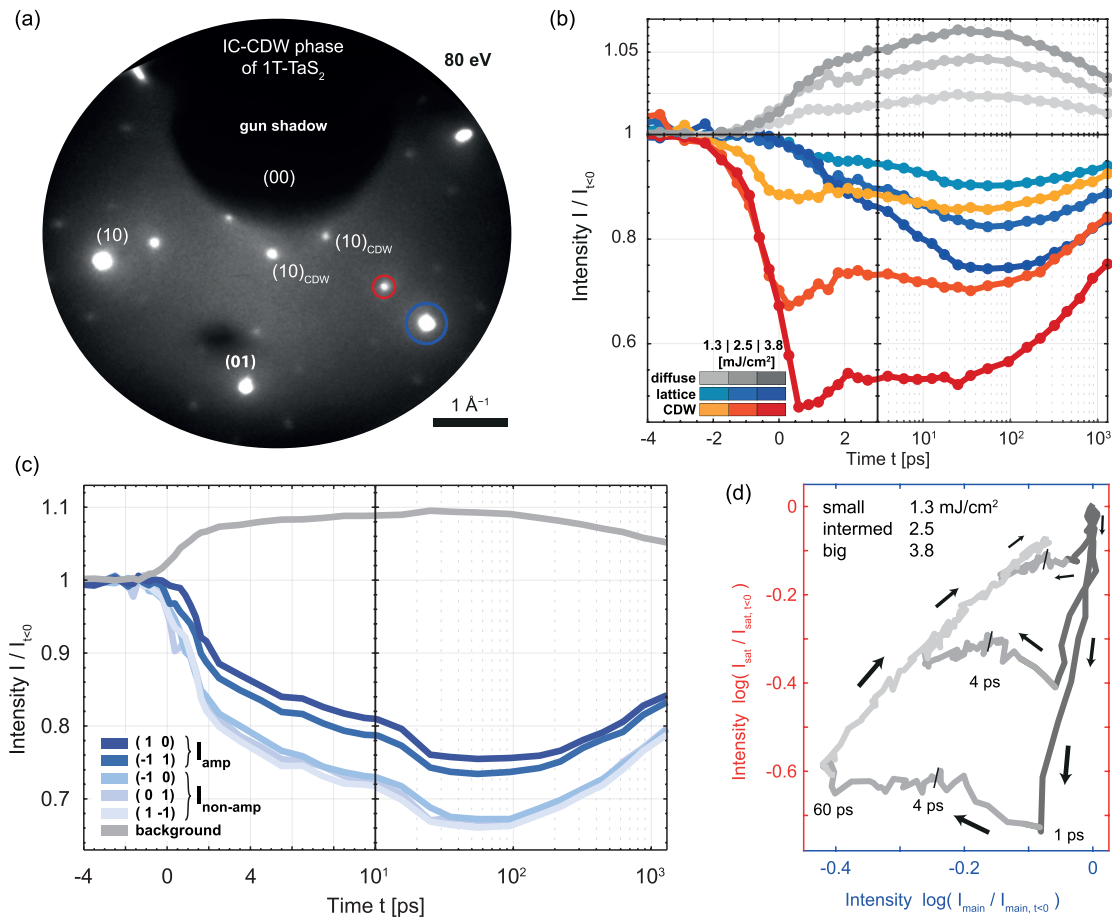

FIG. 9. Measurements in the IC phase for an electron energy of 80 eV. (a) Diffraction pattern of the IC phase of 1T-TaS$_2$ showing main lattice reflexes and first-order PLD-induced satellites (integration time: 90 s). (b) Time-dependent measurement of reflexes [blue and red circles in (a)] and diffuse background (for three fluences). The main lattice signal is averaged over the (10) and (−1 1) spots (blue), the satellite signal over several reflexes. Curves are normalized to the signal at negative times. (c) Time-dependent intensity of visible main lattice reflexes and integrated background intensity, for a fluence of $F = 3.8$ mJ/cm^2. Two inequivalent classes of spot groups are found, but none shows a strong dependence on the amplitude quench. (d) Main lattice intensity vs satellite peak intensity, leading to cyclic trajectories in a 2D plane with varying sizes. Note that all curves reach a common equilibrium line after approximately 60 ps. The gray color scale highlights certain time intervals (dark gray: 0–1 ps, medium, gray: 1–60 ps, and light gray: 60–1500 ps).

dependent Debye–Waller suppression e^{-2W_s} from the intensity of the peaks sensitive to the PLD, with a constant factor $C_1 = 0.81$ that accounts for the slightly different W_s of these peaks:

$$I_{\text{ratio, main},F} = \left(\frac{I_{\text{amp},F}}{I_{\text{non-amp},F_1}}\right)^{\frac{F}{F_1} \cdot C_1} = 1 - c_s A^2. \tag{A3}$$

The value of C_1 was determined by the main peak suppression at long delays (beyond 1 ns) and the lowest fluence ($F_1 = 1.3$ mJ/cm^2), for which a negligible amplitude change is expected. The value of c_s for the amplitude-sensitive peaks is determined from the A^2-intensity dependence of the phonon-corrected satellite peaks [Eq. (3)], evaluated at maximum suppression of the lowest fluence.

From the satellite reflexes (11 brightest spots), the corrected amplitude is obtained similarly using the Debye–Waller–dominated main lattice curve $I_{\text{non-amp},F_1}$ for the lowest fluence with the factor $C_2 = 1.2$:

$$I_{\text{ratio, sat},F} = \left(\frac{I_{\text{sat},F}}{I_{\text{non-amp},F_1}}\right)^{\frac{F}{F_1} \cdot C_2} = A^2. \tag{A4}$$

b. Fitting of time constants

The fit function in Fig. 3(d) is based on a step-like decrease followed by two exponential relaxations,

$$S(t) = 1 - \theta(t - t_0) \cdot \left(-A_1 + A_2 \cdot (1 - e^{-(t-t_0)/\tau})\right)$$
$$+ A_3 \cdot (1 - e^{-(t-t_0)/\tau_2}), \tag{A5}$$

where θ is the Heaviside function, t_0 is time zero, A_1, A_2, and A_3 are the amplitudes, and τ_1 and τ_2 time constants. The complete fit function is the convolution of $S(t)$ with a Gaussian (FWHM of 1 ps) corresponding to the temporal resolution in our experiment.

APPENDIX B: DATA FOR THE NEARLY COMMENSURATE (NC) PHASE

Figure 8 displays the analysis discussed above applied to the nearly commensurate phase. Similar features are found in the pump–probe curves for the main and satellite diffraction peaks, as well as the background [Fig. 8(c)], the long-lived amplitude suppression [Figs. 8(d) and 8(e)], and the relaxation cycles [Fig. 8(f)]. In particular, the two-stage amplitude relaxation process (first stage up to 4 ps and second stage up to 60 ps) is very pronounced at all fluences.

APPENDIX C: DATA AT 80 EV ELECTRON ENERGY

Figure 9 shows additional data recorded in the IC phase at 80 eV energy. The main lattice peaks show a much weaker dependency on the PLD amplitude [Figs. 9(b)–9(d)].

APPENDIX D: RELAXATION CYCLES FOR MAIN PEAKS (−1 1), (0 1), AND (1 −1)

Figure 10 shows the relaxation cycles in the IC phase as in Fig. 5(a), using the intensities of the main lattice peaks (−1 1), (0 1), and (1 −1) without sensitivity to the PLD amplitude.
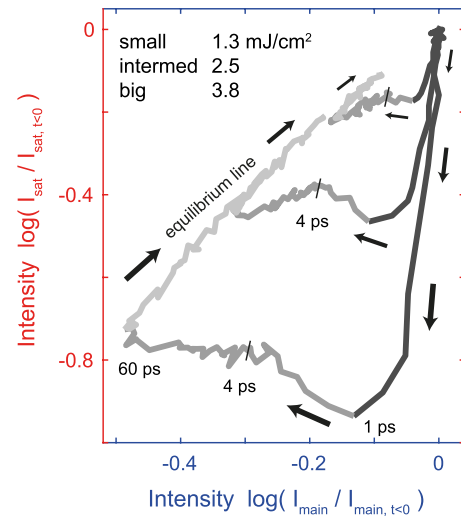

FIG. 10. Main lattice peaks without amplitude features vs satellite peak intensities, leading to cyclic trajectories in a 2D plane with varying sizes. All curves reach a common equilibrium line after approximately 60 ps. The gray color scale highlights certain time intervals (dark gray: 0–1 ps, medium, gray: 1–60 ps, and light gray: 60–1500 ps).

APPENDIX E: IMPACT OF CDW DEFECTS ON PEAK WIDTH

Here, we argue that our data rules out a linear scaling of CDW defect density with fluence and is only consistent with a non-linear or threshold behavior. Assuming a linear relation of the defect density with the fluence $n \sim F$ and a correlation length $L \sim 1/\sqrt{n}$ (see Ref. 35), the defect-induced broadening should scale as $\sigma_{top} \sim 1/L \sim \sqrt{n} \sim \sqrt{F}$. A doubling of the normalized peak widths $\sigma_{tot} = \sqrt{\sigma_0^2 + \sigma_{top}^2}$ with respect to the instrument resolution σ_0 for the highest fluence would then imply considerably higher broadening values for lower fluences ($\sigma_{tot,2.5} = 1.7$ and $\sigma_{tot,1.3} = 1.4$) than observed in our measurement [Fig. 4(c)]. Experimentally, we find maximum broadening values at $t \approx 1$ ps of $\sigma_{tot,3.8} \approx 2$, $\sigma_{tot,2.5} \approx 1.3$, and $\sigma_{tot,1.3} \approx 1$ for the highest, intermediate and lowest fluence, respectively [see Fig. 4(c)]. Thus, we infer that the density of topological defects does not scale linearly with fluence.

APPENDIX F: DYNAMICAL LEED COMPUTATION

We performed dynamical LEED simulations on the commensurate CDW phase of 1T-TaS$_2$ varying the atomic displacements of sulfur and tantalum continuously from the undistorted structure toward the C-phase structure recently reconstructed.[77] We are aware that the C phase is a simple approximation for the description of the high-temperature incommensurate CDW phase. However, it exhibits the same crucial feature of opposing sulfur displacements that we believe is responsible for the different sensitivities of the main lattice peaks. Also, dynamic LEED calculations involve high computational effort, in particular for large unit cells necessary for incommensurate structures. The obtained data

contain PLD-amplitude- and energy-dependent scattering intensities for main lattice and CDW satellite spots. In the following, we focus on main lattice diffraction intensities.

In the electron energy range of 70–140 eV, the diffraction intensity is mainly determined by scattering from sulfur atoms, explaining the strong dependence from the PLD amplitude of sulfur atoms [Fig. 11(a)].

Figure 11(b) shows PLD dependent intensities for electron energies of 100 and 80 eV, each normalized to the intensity value for zero distortion (metal structure). The PLD amplitude range is adapted to the expected values realized in the incommensurate phase,[40] which are assumed to be considerably smaller (∼30% of PLD amplitude of the commensurate low-temperature phase). In this range for 100 eV, we can show that there are two groups of main lattice spots that respond differently upon PLD changes, whereas for 80 eV, all intensities follow a common curve. Moreover, the magnitude of the relative intensity changes approximately matches the observed ones in the experiment. The curves within a group of main lattice peaks [(1 0), (−1 1)] and [(−1 0), (0 1), (1 −1)] coincide since the simulation is performed at normal incidence.

Figure 11(c) shows energy-dependent intensity curves for two main lattice peaks contained in one of the two groups (light and dark blue), each for zero PLD and 30% PLD amplitude of the commensurate low-temperature phase. The ratio of spectra for each
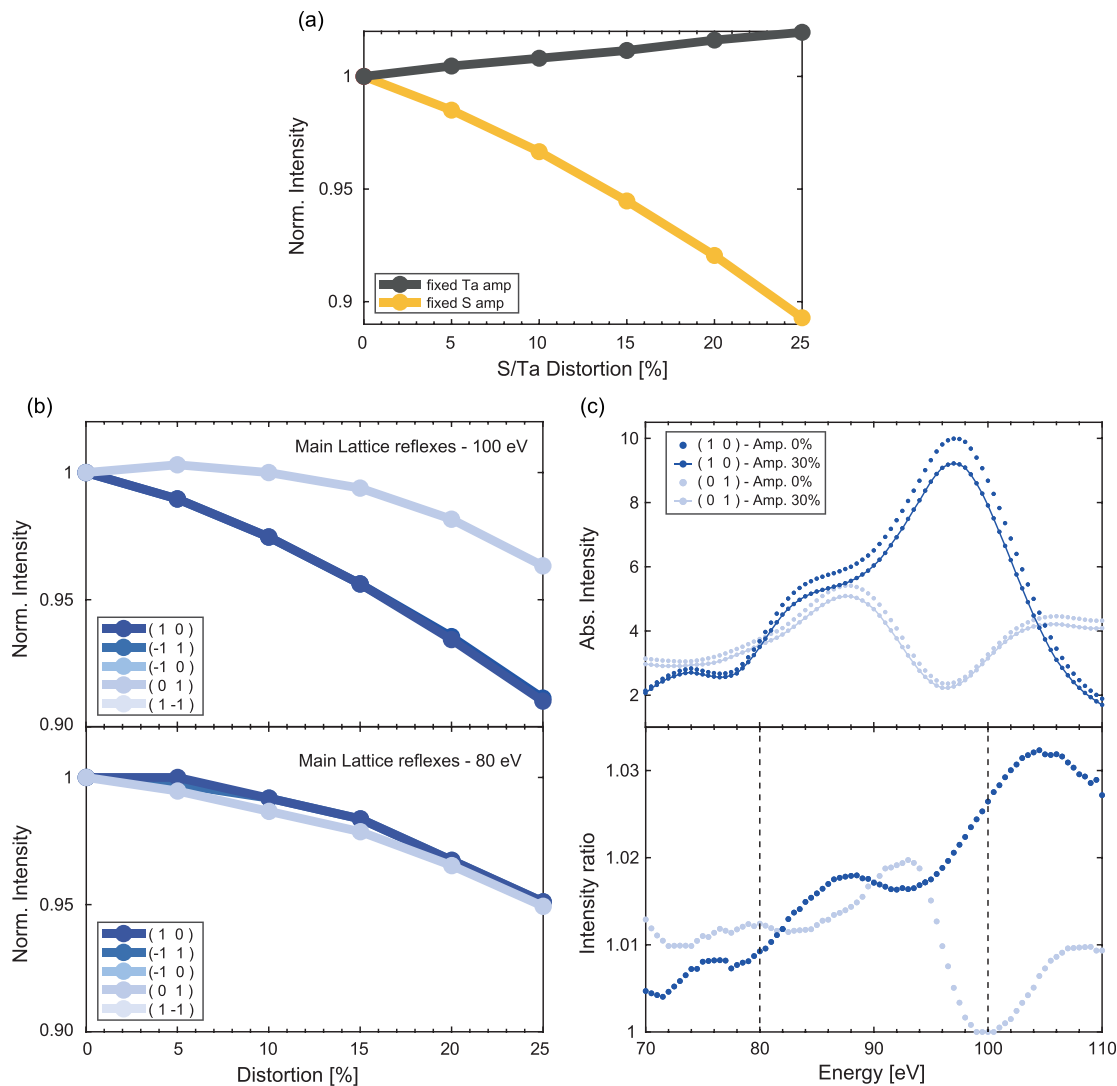

FIG. 11. Dynamical LEED simulations. (a) Normalized intensity of the main lattice reflex (1 0) as a function of sulfur and tantalum displacement for an electron energy of 100 eV. Enhanced scattering of sulfur atoms results in a much stronger dependence on the sulfur atom displacements. (b) Normalized intensities of main lattice spots for electron energies of 80 and 100 eV as a function of the fraction of the maximum commensurate PLD amplitude. The diffraction reflexes split up into two spot groups. Light and dark blue curves coincide, respectively, due to the normal incidence of the electron beam. (c) LEED spectra (top) for both groups (light and dark blue) for vanishing (points) and finite (dash points) distortion. The percentage refers to the amplitude of the commensurate PLD in the low-temperature phase. The intensity ratio (bottom) illustrates the energy-dependent sensitivity between reflex groups.

spot with minimal and maximal amplitudes [Fig. 11(c), bottom] displays a rich oscillatory behavior. Importantly, however, for energies of 80 eV and 100 eV, the spots exhibit a drastically different sensitivity to PLD changes, with a small and large difference for the separate spot groups, respectively. These predictions directly corroborate our experimental findings at different electron beam energies.

REFERENCES

[1]S. Weinberg, *The Quantum Theory of Fields* (Cambridge University Press, 1995).

[2]T. W. B. Kibble, "Topology of cosmic domains and strings," J. Phys. A **9**, 1387–1398 (1976).

[3]W. H. Zurek, "Cosmological experiments in superfluid helium?," Nature **317**, 505–508 (1985).

[4]A. Auerbach, *Interacting Electrons and Quantum Magnetism* (Springer Science & Business Media, 2012).

[5]A. Altland and B. D. Simons, *Condensed Matter Field Theory* (Cambridge University Press, 2010).

[6]P. W. Higgs, "Broken symmetries and the masses of gauge bosons," Phys. Rev. Lett. **13**, 508–509 (1964).

[7]Y. Nambu, "Quasi-particles and gauge invariance in the theory of superconductivity," Phys. Rev. **117**, 648–663 (1960).

[8]J. Goldstone, "Field theories with superconductor solutions," Il Nuovo Cimento **19**, 154–164 (1961).

[9]H. Fröhlich, "On the theory of superconductivity: The one-dimensional case," Proc. R. Soc. Lond., Ser. A **223**, 296–305 (1954).

[10]R. E. Peierls, *Quantum Theory of Solids* (Clarendon Press, 1955).

[11]J. Bardeen, L. N. Cooper, and J. R. Schrieffer, "Theory of superconductivity," Phys. Rev. **108**, 1175–1204 (1957).

[12]G. Grüner, *Density Waves in Solids*, Frontiers in Physics (Addison-Wesley Pub. Co., Advanced Book Program, Reading, MA, 1994), Vol. 89.

[13]L. D. Chapman and R. Colella, "Experimental evidence from x-ray diffraction for phase excitations in solids," Phys. Rev. Lett. **52**, 652–655 (1984).

[14]W. Minor, L. D. Chapman, S. N. Ehrlich, and R. Colella, "Phason velocities in TaS$_2$ by x-ray diffuse scattering," Phys. Rev. B **39**, 1360–1362 (1989).

[15]J. P. Pouget, B. Hennion, C. Escribe-Filippini, and M. Sato, "Neutron-scattering investigations of the Kohn anomaly and of the phase and amplitude charge-density-wave excitations of the blue bronze K$_{0.3}$MoO$_3$," Phys. Rev. B **43**, 8421–8430 (1991).

[16]G.-H. Gweon, J. D. Denlinger, J. A. Clack, J. W. Allen, C. G. Olson, E. DiMasi, M. C. Aronson, B. Foran, and S. Lee, "Direct observation of complete fermi surface, imperfect nesting, and gap anisotropy in the high-temperature incommensurate charge-density-wave compound SmTe$_3$," Phys. Rev. Lett. **81**, 886–889 (1998).

[17]S. Uchida and S. Sugai, "Infrared and Raman studies on commensurate CDW states in transition metal dichalcogenides," Physica B+C **105**, 393–399 (1981).

[18]T. Hirata and F. Ohuchi, "Temperature dependence of the Raman spectra of 1T-TaS$_2$," Solid State Commun. **117**, 361–364 (2001).

[19]J. Duffey, R. Kirby, and R. Coleman, "Raman scattering from 1T-TaS$_2$," Solid State Commun. **20**, 617–621 (1976).

[20]S. Hellmann, M. Beye, C. Sohrt, T. Rohwer, F. Sorgenfrei, H. Redlin, M. Kalläne, M. Marczynski-Bühlow, F. Hennies, M. Bauer, A. Föhlisch, L. Kipp, W. Wurth, and K. Rossnagel, "Ultrafast melting of a charge-density wave in the Mott insulator 1T-TaS$_2$," Phys. Rev. Lett. **105**, 187401 (2010).

[21]L. Perfetti, P. A. Loukakos, M. Lisowski, U. Bovensiepen, M. Wolf, H. Berger, S. Biermann, and A. Georges, "Femtosecond dynamics of electronic states in the Mott insulator 1T-TaS$_2$ by time resolved photoelectron spectroscopy," New J. Phys. **10**, 053019 (2008).

[22]H. Y. Liu, I. Gierz, J. C. Petersen, S. Kaiser, A. Simoncig, A. L. Cavalieri, C. Cacho, I. C. E. Turcu, E. Springate, F. Frassetto, L. Poletto, S. S. Dhesi, Z.-A. Xu, T. Cuk, R. Merlin, and A. Cavalleri, "Possible observation of parametrically amplified coherent phasons in K$_{0.3}$MoO$_3$ using time-resolved extreme-ultraviolet angle-resolved photoemission spectroscopy," Phys. Rev. B **88**, 045104 (2013).

[23]J. C. Petersen, S. Kaiser, N. Dean, A. Simoncig, H. Y. Liu, A. L. Cavalieri, C. Cacho, I. C. E. Turcu, E. Springate, F. Frassetto, L. Poletto, S. S. Dhesi, H. Berger, and A. Cavalleri, "Clocking the melting transition of charge and lattice order in 1T-TaS$_2$ with ultrafast extreme-ultraviolet angle-resolved photoemission spectroscopy," Phys. Rev. Lett. **107**, 177402 (2011).

[24]L. Perfetti, P. A. Loukakos, M. Lisowski, U. Bovensiepen, H. Berger, S. Biermann, P. S. Cornaglia, A. Georges, and M. Wolf, "Time evolution of the electronic structure of 1T-TaS$_2$ through the insulator-metal transition," Phys. Rev. Lett. **97**, 067402 (2006).

[25]C. Sohrt, A. Stange, M. Bauer, and K. Rossnagel, "How fast can a Peierls–Mott insulator be melted?," Faraday Discuss. **171**, 243–257 (2014).

[26]J. Demsar, L. Forró, H. Berger, and D. Mihailovic, "Femtosecond snapshots of gap-forming charge-density-wave correlations in quasi-two-dimensional dichalcogenides 1T-TaS$_2$ and 2H-TaSe$_2$," Phys. Rev. B **66**, 041101 (2002).

[27]M. Eichberger, H. Schäfer, M. Krumova, M. Beyer, J. Demsar, H. Berger, G. Moriena, G. Sciaini, and R. J. D. Miller, "Snapshots of cooperative atomic motions in the optical suppression of charge density waves," Nature **468**, 799–802 (2010).

[28]N. Erasmus, M. Eichberger, K. Haupt, I. Boshoff, G. Kassier, R. Birmurske, H. Berger, J. Demsar, and H. Schwoerer, "Ultrafast dynamics of charge density waves in 4Hb-TaSe$_2$ probed by femtosecond electron diffraction," Phys. Rev. Lett. **109**, 167402 (2012).

[29]C. Laulhé, L. Cario, B. Corraze, E. Janod, T. Huber, G. Lantz, S. Boulfaat, A. Ferrer, S. Mariager, J. Johnson, S. Grübel, A. Lübcke, G. Ingold, P. Beaud, S. Johnson, and S. Ravy, "X-ray study of femtosecond structural dynamics in the 2D charge density wave compound 1T-TaS$_2$," Physica B **460**, 100–104 (2015).

[30]T.-R. T. Han, Z. Tao, S. D. Mahanti, K. Chang, C.-Y. Ruan, C. D. Malliakas, and M. G. Kanatzidis, "Structural dynamics of two-dimensional charge-density waves in CeTe$_3$ investigated by ultrafast electron crystallography," Phys. Rev. B **86**, 075145 (2012).

[31]C. W. Nicholson, A. Lücke, W. G. Schmidt, M. Puppin, L. Rettig, R. Ernstorfer, and M. Wolf, "Beyond the molecular movie: Dynamics of bands and bonds during a photoinduced phase transition," Science **362**, 821–825 (2018).

[32]X. Shi, W. You, Y. Zhang, Z. Tao, P. M. Oppeneer, X. Wu, R. Thomale, K. Rossnagel, M. Bauer, H. Kapteyn, and M. Murnane, "Ultrafast electron calorimetry uncovers a new long-lived metastable state in 1T-TaSe$_2$ mediated by mode-selective electron-phonon coupling," Sci. Adv. **5**, eaav4449 (2019).

[33]K. Haupt, M. Eichberger, N. Erasmus, A. Rohwer, J. Demsar, K. Rossnagel, and H. Schwoerer, "Ultrafast metamorphosis of a complex charge-density wave," Phys. Rev. Lett. **116**, 016402 (2016).

[34]T.-R. T. Han, *Ultrafast Electron Crystallography Studies of Charge-Density Waves Materials and Nanoscale Ice* (Michigan State University, 2015).

[35]S. Vogelgesang, G. Storeck, J. G. Horstmann, T. Diekmann, M. Sivis, S. Schramm, K. Rossnagel, S. Schäfer, and C. Ropers, "Phase ordering of charge density waves traced by ultrafast low-energy electron diffraction," Nat. Phys. **14**, 184–190 (2018).

[36]G. Lantz, C. Laulhé, S. Ravy, M. Kubli, M. Savoini, K. Tasca, E. Abreu, V. Esposito, M. Porer, A. Ciavardini, L. Cario, J. Rittmann, P. Beaud, and S. L. Johnson, "Domain-size effects on the dynamics of a charge density wave in 1T-TaS$_2$," Phys. Rev. B **96**, 224101 (2017).

[37]M. Gulde, S. Schweda, G. Storeck, M. Maiti, H. K. Yu, A. M. Wodtke, S. Schafer, and C. Ropers, "Ultrafast low-energy electron diffraction in transmission resolves polymer/graphene superstructure dynamics," Science **345**, 200–204 (2014).

[38]G. Storeck, S. Vogelgesang, M. Sivis, S. Schäfer, and C. Ropers, "Nanotip-based photoelectron microgun for ultrafast LEED," Struct. Dyn. **4**, 044024 (2017).

[39]J. G. Horstmann, B. Wit, G. Storeck, and C. Ropers, "Coherent control of a structural phase transition in a solid-state surface system," arXiv:1906.11155 (2019).

[40]C. B. Scruby, P. M. Williams, and G. S. Parry, "The role of charge density waves in structural transformations of 1T-TaS$_2$," Philos. Mag. **31**, 255–274 (1975).

[41]A. Spijkerman, J. L. de Boer, A. Meetsma, G. A. Wiegers, and S. van Smaalen, "X-ray crystal-structure refinement of the nearly commensurate phase of 1T-TaS$_2$ in (3 + 2)-dimensional superspace," Phys. Rev. B **56**, 13757–13767 (1997).

[42]I. Vaskivskyi, J. Gospodaric, S. Brazovskii, D. Svetin, P. Sutar, E. Goreshnik, I. A. Mihailovic, T. Mertelj, and D. Mihailovic, "Controlling the metal-to-

insulator relaxation of the metastable hidden quantum state in 1T-TaS₂," Sci. Adv. **1**, e1500168 (2015).

⁴³S. Hellmann, T. Rohwer, M. Kalläne, K. Hanff, C. Sohrt, A. Stange, A. Carr, M. Murnane, H. Kapteyn, L. Kipp, M. Bauer, and K. Rossnagel, "Time-domain classification of charge-density-wave insulators," Nat. Commun. **3**, 1069 (2012).

⁴⁴P. Fazekas and E. Tosatti, "Electrical, structural and magnetic properties of pure and doped 1T-TaS₂," Philos. Mag. B **39**, 229–244 (1979).

⁴⁵P. Darancet, A. J. Millis, and C. A. Marianetti, "Three-dimensional metallic and two-dimensional insulating behavior in octahedral tantalum dichalcogenides," Phys. Rev. B **90**, 045134 (2014).

⁴⁶K. T. Law and P. A. Lee, "1T-TaS₂ as a quantum spin liquid," Proc. Nat. Acad. Sci. **114**, 6996–7000 (2017).

⁴⁷K. Rossnagel, "On the origin of charge-density waves in select layered transition-metal dichalcogenides," J. Phys. **23**, 213001 (2011).

⁴⁸B. Sipos, A. F. Kusmartseva, A. Akrap, H. Berger, L. Forró, and E. Tutiš, "From Mott state to superconductivity in 1T-TaS₂," Nat. Mater. **7**, 960–965 (2008).

⁴⁹L. Stojchevska, I. Vaskivskyi, T. Mertelj, P. Kusar, D. Svetin, S. Brazovskii, and D. Mihailovic, "Ultrafast switching to a stable hidden quantum state in an electronic crystal," Science **344**, 177–180 (2014).

⁵⁰T. Ritschel, J. Trinckauf, K. Koepernik, B. Büchner, M. V. Zimmermann, H. Berger, Y. I. Joe, P. Abbamonte, and J. Geck, "Orbital textures and charge density waves in transition metal dichalcogenides," Nat. Phys. **11**, 328–331 (2015).

⁵¹M. Klanjšek, A. Zorko, R. Žitko, J. Mravlje, Z. Jagličć, P. Biswas, P. Prelovšek, D. Mihailovic, and D. Arčon, "A high-temperature quantum spin liquid with polaron spins," Nat. Phys. **13**, 1130–1134 (2017).

⁵²B. Dardel, M. Grioni, D. Malterre, P. Weibel, Y. Baer, and F. Lévy, "Spectroscopic signatures of phase transitions in a charge-density-wave system: 1 T-TaS₂," Phys. Rev. B **46**, 7407–7412 (1992).

⁵³K. Nakanishi, H. Takatera, Y. Yamada, and H. Shiba, "The nearly commensurate phase and effect of harmonics on the successive phase transition in 1T-TaS₂," J. Phys. Soc. Jpn. **43**, 1509–1517 (1977).

⁵⁴K. Nakanishi and H. Shiba, "Domain-like incommensurate charge-density-wave states and the first-order incommensurate-commensurate transitions in layered tantalum dichalcogenides. I. 1T-polytype," J. Phys. Soc. Jpn. **43**, 1839–1847 (1977).

⁵⁵T. Ishiguro and H. Sato, "High-resolution electron microscopy of discommensuration in the nearly commensurate phase on warming of 1T-TaS₂," Phys. Rev. B **52**, 759–765 (1995).

⁵⁶C. Laulhé, T. Huber, G. Lantz, A. Ferrer, S. Mariager, S. Grübel, J. Rittmann, J. Johnson, V. Esposito, A. Lübcke, L. Huber, M. Kubli, M. Savoini, V. Jacques, L. Cario, B. Corraze, E. Janod, G. Ingold, P. Beaud, S. Johnson, and S. Ravy, "Ultrafast formation of a charge density wave state in 1T-TaS₂: Observation at nanometer scales using time-resolved x-ray diffraction," Phys. Rev. Lett. **118**, 247401 (2017).

⁵⁷L. Le Guyader, T. Chase, A. H. Reid, R. K. Li, D. Svetin, X. Shen, T. Vecchione, X. J. Wang, D. Mihailovic, and H. A. Dürr, "Stacking order dynamics in the quasi-two-dimensional dichalcogenide 1T-TaS₂ probed with MeV ultrafast electron diffraction," Struct. Dyn. **4**, 044020 (2017).

⁵⁸I. Avigo, P. Zhou, M. Kalläne, K. Rossnagel, U. Bovensiepen, and M. Ligges, "Excitation and relaxation dynamics of the photo-perturbed correlated electron system 1T-TaS₂," Appl. Sci. **9**, 44 (2019).

⁵⁹A. Zong, A. Kogar, Y.-Q. Bie, T. Rohwer, C. Lee, E. Baldini, E. Ergeçen, M. B. Yilmaz, B. Freelon, E. J. Sie, H. Zhou, J. Straquadine, P. Walmsley, P. E. Dolgirev, A. V. Rozhkov, I. R. Fisher, P. Jarillo-Herrero, B. V. Fine, and N. Gedik, "Evidence for topological defects in a photoinduced phase transition," Nat. Phys. **15**, 27–31 (2019).

⁶⁰P. Kusar, T. Mertelj, V. V. Kabanov, J.-H. Chu, I. R. Fisher, H. Berger, L. Forró, and D. Mihailovic, "Anharmonic order-parameter oscillations and lattice coupling in strongly driven 1T-TaS₂ and TbTe₃ charge-density-wave compounds: A multiple-pulse femtosecond laser spectroscopy study," Phys. Rev. B **83**, 035104 (2011).

⁶¹A. Mann, E. Baldini, A. Odeh, A. Magrez, H. Berger, and F. Carbone, "Probing the coupling between a doublon excitation and the charge-density wave in TaS₂ by ultrafast optical spectroscopy," Phys. Rev. B **94**, 115122 (2016).

⁶²W. L. McMillan, "Landau theory of charge-density waves in transition-metal dichalcogenides," Phys. Rev. B **12**, 1187–1196 (1975).

⁶³W. L. McMillan, "Theory of discommensurations and the commensurate-incommensurate charge-density-wave phase transition," Phys. Rev. B **14**, 1496–1502 (1976).

⁶⁴A. W. Overhauser, "Observability of charge-density waves by neutron diffraction," Phys. Rev. B **3**, 3173 (1971).

⁶⁵G. F. Giuliani and A. W. Overhauser, "Structure factor of a charge-density wave," Phys. Rev. B **23**, 3737–3743 (1981).

⁶⁶Y. R. Wang and A. W. Overhauser, "Thermal-diffuse scattering of x rays by phasons," Phys. Rev. B **39**, 1357–1359 (1989).

⁶⁷A. Ichimiya and P. I. Cohen, *Reflection High-Energy Electron Diffraction* (Cambridge University Press, Cambridge, UK/New York, 2004).

⁶⁸J. Li, J. Li, K. Sun, L. Wu, H. Huang, R. Li, J. Yang, X. Wang, H. Luo, R. J. Cava, I. K. Robinson, Y. Zhu, and J. Tao, "Ultrafast decoupling of atomic sublattices in a charge-density-wave material," arXiv:1903.09911 (2019).

⁶⁹M. A. Van Hove, W. H. Weinberg, and C.-M. Chan, *Low-Energy Electron Diffraction: Experiment, Theory and Surface Structure Determination*, Springer Series in Surface Sciences Vol. 6, 1st ed. (Springer, Berlin, 1986).

⁷⁰M. J. Stern, L. P. René de Cotret, M. R. Otto, R. P. Chatelain, J.-P. Boisvert, M. Sutton, and B. J. Siwick, "Mapping momentum-dependent electron-phonon coupling and nonequilibrium phonon dynamics with ultrafast electron diffuse scattering," Phys. Rev. B **97**, 165416 (2018).

⁷¹L. Waldecker, R. Bertoni, H. Hübener, T. Brumme, T. Vasileiadis, D. Zahn, A. Rubio, and R. Ernstorfer, "Momentum-resolved view of electron-phonon coupling in multilayer WSe₂," Phys. Rev. Lett. **119**, 036803 (2017).

⁷²M. R. Otto, J.-H. Pöhls, L. P. R. de Cotret, M. J. Stern, M. Sutton, and B. J. Siwick, "Ultrafast signatures of exciton-phonon coupling in TiSe₂," arXiv:1912.03559 (2019).

⁷³W. Lee, Y. Chuang, R. Moore, Y. Zhu, L. Patthey, M. Trigo, D. Lu, P. Kirchmann, O. Krupin, M. Yi, M. Langner, N. Huse, J. Robinson, Y. Chen, S. Zhou, G. Coslovich, B. Huber, D. Reis, R. Kaindl, R. Schoenlein, D. Doering, P. Denes, W. Schlotter, J. Turner, S. Johnson, M. Först, T. Sasagawa, Y. Kung, A. Sorini, A. Kemper, B. Moritz, T. Devereaux, D.-H. Lee, Z. Shen, and Z. Hussain, "Phase fluctuations and the absence of topological defects in a photo-excited charge-ordered nickelate," Nat. Commun. **3**, 838 (2012).

⁷⁴X. Gu and R. Yang, "Phonon transport in single-layer transition metal dichalcogenides: A first-principles study," Appl. Phys. Lett. **105**, 131903 (2014).

⁷⁵M. Mohr, J. Maultzsch, E. Dobardžić, S. Reich, I. Milošević, M. Damnjanović, A. Bosak, M. Krisch, and C. Thomsen, "Phonon dispersion of graphite by inelastic x-ray scattering," Phys. Rev. B **76**, 035439 (2007).

⁷⁶"Note that the different behavior of these inequivalent peaks is unrelated to a potential decoupling of atomic sublattices, as reported in Ref. 68 based on different groups of peaks. In fact, the diffraction signal is inherently mostly affected by the sulfur atoms due to the much larger atomic scattering factors at 100 eV energy."

⁷⁷G. von Witte, T. Kißlinger, J. G. Horstmann, K. Rossnagel, M. A. Schneider, C. Ropers, and L. Hammer, "Surface structure and stacking of the commensurate $(\sqrt{13} \times \sqrt{13})$R13.9° charge density wave phase of 1T-TaS₂ (0001)," Phys. Rev. B **100**, 155407 (2019).

⁷⁸M. Eichberger, "Probing structural dynamics in dichalcogenides with ultrashort electron pulses," Ph.D. thesis (Universität Konstanz, 2014).

⁷⁹M. Ligges, I. Avigo, D. Golež, H. Strand, Y. Beyazit, K. Hanff, F. Diekmann, L. Stojchevska, M. Kalläne, P. Zhou, K. Rossnagel, M. Eckstein, P. Werner, and U. Bovensiepen, "Ultrafast doublon dynamics in photoexcited 1T-TaS₂," Phys. Rev. Lett. **120**, 166401 (2018).

⁸⁰M. Trigo, M. Fuchs, J. Chen, M. P. Jiang, M. Cammarata, S. Fahy, D. M. Fritz, K. Gaffney, S. Ghimire, A. Higginbotham, S. L. Johnson, M. E. Kozina, J. Larsson, J. Lemke, A. M. Lindenberg, G. Ndabashimiye, F. Quirin, K. Sokolowski-Tinten, C. Uher, G. Wang, J. S. Wark, D. Zhu, and D. A. Reis, "Fourier-transform inelastic X-ray scattering from time- and momentum-dependent phonon–phonon correlations," Nat. Phys. **9**, 790–794 (2013).

⁸¹M. Harb, H. Enquist, A. Jurgilaitis, F. T. Tuyakova, A. N. Obraztsov, and J. Larsson, "Phonon-phonon interactions in photoexcited graphite studied by ultrafast electron diffraction," Phys. Rev. B **93**, 104104 (2016).

⁸²M. A. Krivoglaz, *Diffuse Scattering of X-Rays and Neutrons by Fluctuations* (Springer, Berlin, 1996).

⁸³J. D. Axe, "Debye-Waller factors for incommensurate structures," Phys. Rev. B **21**, 4181–4190 (1980).

[84]W. Adlhart, "Dynamic structure factors for excitations in modulated structures," Acta Crystallogr., Sect. A **38**, 498–504 (1982).

[85]T. Aslanyan, T. Shigenari, and K. Abe, "Debye-Waller factors for incommensurate structures," J. Phys. **10**, 4565 (1998).

[86]T. A. Aslanyan, T. Shigenari, and K. Abe, "Comment on the Debye-Waller factors for incommensurate structures," arXiv:cond-mat/0502638 (2005).

[87]A. Kogar, A. Zong, P. E. Dolgirev, X. Shen, J. Straquadine, Y.-Q. Bie, X. Wang, T. Rohwer, I.-C. Tung, Y. Yang, R. Li, J. Yang, S. Weathersby, S. Park, M. E. Kozina, E. J. Sie, H. Wen, P. Jarillo-Herrero, I. R. Fisher, X. Wang, and N. Gedik, "Light-induced charge density wave in LaTe$_3$," Nat. Phys. **16**, 159–163 (2020).

[88]P. A. Lee, T. M. Rice, and P. W. Anderson, "Fluctuation effects at a Peierls transition," Phys. Rev. Lett. **31**, 462–465 (1973).

[89]R. H. McKenzie and J. W. Wilkins, "Effect of lattice zero-point motion on electronic properties of the Peierls-Fröhlich state," Phys. Rev. Lett. **69**, 1085–1088 (1992).

[90]L. Degiorgi, G. Grüner, K. Kim, R. H. McKenzie, and P. Wachter, "Optical probing of thermal lattice fluctuations in charge-density-wave condensates," Phys. Rev. B **49**, 14754–14757 (1994).

[91]H. Monien, "Exact results for the crossover from Gaussian to Non-Gaussian order parameter fluctuations in quasi-one-dimensional electronic systems," Phys. Rev. Lett. **87**, 126402 (2001).

[92]K. Nakanishi and H. Shiba, "Domain-like incommensurate charge-density-wave states and the first-order incommensurate-commensurate transitions in layered tantalum dichalcogenides. II. 2H-polytype," J. Phys. Soc. Jpn. **44**, 1465 (1978).